33RD CONGRESS
OF THE INTERNATIONAL COUNCIL
OF THE AERONAUTICAL SCIENCES
STOCKHOLM, SWEDEN, 4–9 SEPTEMBER, 2022

ICAS 2022 SWEDEN

NUMERICAL INVESTIGATION ON THE DOUBLE TRANSONIC DIP OF SUPERCRITICAL AIRFOIL FLUTTER

Toma Miyake[1] and Hiroshi Terashima[1]

[1]Hokkaido University, Kita 13, Nishi 8, Kita-ku, Sapporo, Hokkaido, Japan.

Abstract

This study numerically investigated the transonic flutter characteristics of a supercritical airfoil. An SC2-0610 supercritical airfoil was used for investigation, and the flutter characteristics were compared with those of a conventional symmetric NACA64A010 airfoil. The study captured a double transonic dip trend in the flutter boundary of the supercritical airfoil. While the first transonic dip, which corresponded to a classical one, was seen with both airfoils, the second transonic dip only emerged with the supercritical airfoil. The second transonic dip was caused by the unsteady behaviors of flow separation and reattachment over the unique lower surface shape of the supercritical airfoil. An analysis using a forced-oscillation airfoil demonstrated that the flow separation and reattachment cycle during the airfoil oscillation produced the phase delay of aerodynamic forces.

Keywords: Supercritical airfoil, Transonic flutter, Double transonic dip, Flow separation and reattachment

1. Introduction

Wing flutter is a self-induced oscillation caused by the coupling of aerodynamic, structural, and inertial forces [1]. When an external force acts on a wing, a phase difference may occur between the structural and aerodynamic forces. If energy is continuously supplied to the wing, the oscillation amplitude may increase with time, which may eventually cause severe damage to the wing structure. In particular, it is known that flutter speed decreases rapidly in the transonic region due to shock appearance on the airfoil surface (which is commonly called transonic dip) [2,3].

There have been experimental and computational studies on the transonic flutter characteristics of conventional symmetric airfoils [4-8]. For the supercritical airfoil, flutter characteristics may change due to the unique airfoil geometry, such as a flat top surface and a positive camber near the trailing edge. One notable characteristic may be the generation of a double transonic dip on the flutter boundary [9]. Yate [9] conducted a transonic flutter experiment using a supercritical airfoil and showed that the double transonic dip interestingly appeared in the flutter boundary with a specific angle of attack condition. However, detailed mechanisms for the double transonic dip have not been discussed.

The present study aims at clarifying the double transonic dip mechanism possibly occurred with a supercritical airfoil. Two-dimensional airfoil flutter simulations were performed using symmetric and supercritical airfoils for investigation.

2. Numerical methods

2.1 Aerodynamics

The Reynolds-averaged two-dimensional compressible Navier–Stokes equations were used to simulate the unsteady flow fields around the airfoils. The inviscid numerical flux was evaluated using the simple high-resolution upwind scheme (SHUS) [10], and a higher-order spatial accuracy was achieved using the monotone upstream-centered scheme for conservation laws (MUSCL) [11] and the van Albada limiter [12]. The lower-upper symmetric Gauss-Seidel (LU-SGS) algorithm [13] was used for the time integration. The Spalart–Allmaras (SA) one-equation model [14] was used for the turbulence model.

At the inflow boundary, all variables were specified as the freestream value. At the outflow boundary,

the pressure was fixed as the freestream value, and the other variables were extrapolated. At the wall, the density was extrapolated and the velocity corresponded to the grid velocity given by the airfoil movement. The normal momentum equation, which includes the effects of wall acceleration on the pressure gradients, was used to determine the pressure at the wall.

2.2 Structural dynamics

Figure 1 shows a structural model that simulates a typical airfoil motion of a swept-back wing [8]. The airfoil owns two-degree-of-freedom: vertical displacement h (downward is positive) and pitching angle α (nose-up is positive). The non-dimensionalized governing equations using half of the wing chord length $b = c/2$ ($\bar{h} = h/b$) and an uncoupled circular pitching frequency ω_α. of the structural model are written as follows [1,8]:

$$[M]\{\ddot{q}\} + [K]\{q\} = \{Q\}, \tag{1}$$

where

$$[M] = \begin{bmatrix} 1 & x_\alpha \\ x_\alpha & {r_\alpha}^2 \end{bmatrix}, \quad [K] = \begin{bmatrix} (\omega_h/\omega_\alpha)^2 & 0 \\ 0 & {r_\alpha}^2 \end{bmatrix}, \quad \{q\} = \begin{Bmatrix} \bar{h} \\ \alpha \end{Bmatrix}, \quad \{Q\} = \frac{{V_*}^2}{\pi}\begin{Bmatrix} -C_l \\ 2C_m \end{Bmatrix}, \tag{2}$$

and

$$V_* = \frac{U_\infty}{b\omega_\alpha\sqrt{\mu}}, \quad \mu = \frac{m}{\rho_\infty b^2 \pi}. \tag{3}$$

In the above equations, ω_h is the uncoupled circular bending frequency. x_α and r_α^2 are the static imbalance and radius of gyration. C_l and C_m are the lift and moment coefficients. V_* is the flutter speed index and μ is the mass ratio. m is the mass per unit length. U_∞ is the freestream velocity, ρ_∞ is the freestream density. In this study, no structural damping is considered.

The asymmetric upper and lower shapes of the SC2-0610 supercritical airfoil generate non-zero lift and moment forces at the beginning of flutter calculations. Therefore, this study modified the force vector $\{Q\}$ of the structural equations using the lift coefficient $C_{l,0}$ and moment coefficient $C_{m,0}$ obtained in the steady-state calculation as follows:

$$\{Q\} = \frac{{V_*}^2}{\pi}\begin{Bmatrix} -(C_l - C_{l,0}) \\ 2(C_m - C_{m,0}) \end{Bmatrix}. \tag{4}$$

This modification allows the airfoil to be initially balanced at any angle of attack of interest.

The fourth-order Runge–Kutta (R–K) method was employed as the time-integration method of the structural equation. The aerodynamic forces C_l and C_m were assumed to be constant at each stage of the R–K method.

2.3 Fluid-structure coupling

Each governing equation was solved separately in the temporal direction, and the variables were exchanged between the fluid and structural equations at each time step (a weak coupling). The procedure of fluid-structure coupling is as follows:

0. Steady-state calculations are performed to obtain the flow field around the airfoil
1. Small displacement is given for initiating an airfoil motion and the airfoil grid is moved
2. The Navier-Stokes equations are solved to obtain the aerodynamic forces
3. The aerodynamic forces are substituted into the structural equations to obtain the displacement h and pitching angle α
4. The airfoil grid is moved using the obtained displacement and pitching angle

Items 2 to 4 are repeated. This study determined the flutter boundary with the time history of airfoil displacement.

2.4 Conditions

In this study, NACA64A010 and SC2-0610 airfoils were used. Figure 2 shows the computational grid for the SC2-0610 airfoil. The grid points was 803 × 150 for the NACA64A010 airfoil and 903 × 150 for the SC2-0610 airfoil, respectively. The minimum grid spacing was 10^{-6} (non-dimensionalized by the chord length c). The outer boundary was placed far away from the airfoil surface at a distance of $30c$ to minimize the boundary effect in the transonic flow simulations. $c(= 2b)$ is the chord length. The time step size was set to $\Delta t_{\text{fluid}} = 10^{-3}$(non-dimensionalized by the chord length and speed of sound).

All grid points were moved according to the airfoil displacement and pitching angle obtained from the structural equations in the flutter calculations. The angle of attack was set to zero.

The structural parameters in Eq. (2) and Fig. 1 are $x_\alpha = 1.8, r_\alpha^2 = 3.48, a = -2.0, \mu = 60$, and $\omega_h = \omega_\alpha = 100$ rad/s [8]. The flutter speed index V_* was parametrically changed to determine the flutter boundary. An eigenvalue analysis of the structural model indicates that the airfoil owns the first bending mode with the natural frequency of 11.35 Hz and the second torsion mode with the natural frequency of 84.95 Hz.

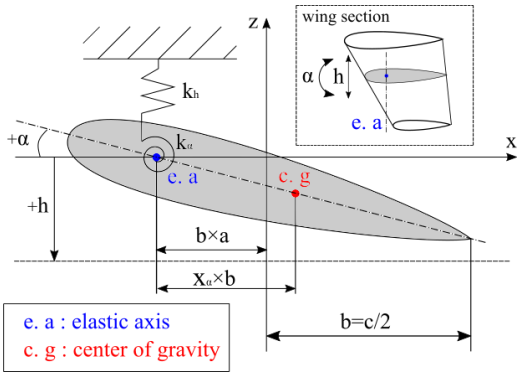

Fig. 1 – Typical wing section model with two-degrees-of-freedom

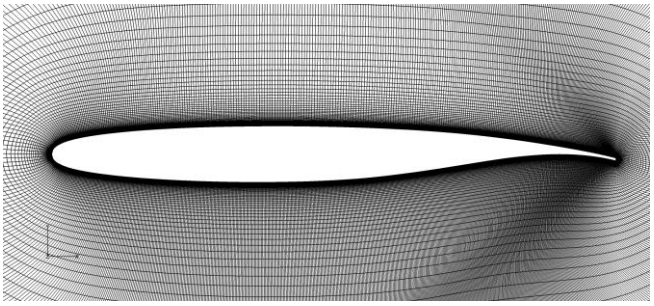

Fig. 2 – Computational grid for the SC2-0610 airfoil

3. Results and discussions

3.1 Flutter characteristics of each airfoil

Figure 3 shows the flutter speed and flutter frequency for both airfoils. In this study, the flutter speed is defined as the value of V_* at the moment when the airfoil oscillation amplitude is nearly constant, and the flutter frequency is the one at the condition. For the NACA64A010 airfoil, the flutter speed takes a minimum value at $M_\infty = 0.825$, and the flutter frequency indicates that the airfoil oscillates in the first bending mode. The flutter speed elevates rapidly in increasing the Mach number, and the bending-torsion coupling mode becomes dominant in the flutter oscillations. These trends represent the typical transonic flutter characteristics reported in several studies [4,8].

On the other hand, the flutter boundary of the SC2-0610 airfoil exhibits the double transonic dip trend. The first dip occurs at a low Mach number condition of $M_\infty = 0.75$, and the second one is generated at a high Mach number condition of $M_\infty = 0.855$. The first dip is caused by the shock wave appearance over the upper surface, as confirmed with the Mach number distributions shown in Fig. 4(a) (the shock wave is not strong but emerges in the forward region). The phase-delayed motion of the shock wave against the airfoil motion produces the negative damping force and reduces the flutter speed [8]. After the first dip, the flutter speed turns to increase in increasing the Mach number. The increase in flutter speed is caused by the flow separation behind the shock wave. As shown in Fig. 4(b), the separation occurs behind the shock wave in increasing the Mach number. In contrast to the shock wave motion with no separation, the shock wave motion with separation may have positive damping against airfoil motions because the shock wave motion was significantly changed with the separation during oscillations [15].

Then, the flutter speed interestingly starts to decrease again in increasing the Mach number. The decrease is primarily caused by the shock wave appearance over the lower surface. Figure 5 shows the Mach number distributions of three Mach number conditions. While the flow fields on the upper surface are similar for three conditions, the flow fields over the lower surface are significantly different in the shock wave and flow separation. In increasing the Mach number, the shock wave emerging over the lower surface is strengthened, and the separation region is accordingly developed.

Figure 6 shows the skin friction distributions over the lower surface, which demonstrate that the boundary layer behind the shock wave is fully separated at a high Mach number condition of $M_\infty = 0.875$, while no separation occurs at a low Mach number condition of $M_\infty = 0.825$. The boundary layer at $M_\infty = 0.855$ (the bottom of the second dip) is partially separated and reattached at a region near the trailing edge. Therefore, the results indicate that the behaviors of boundary-layer separation and reattachment over the lower surface may determine the bottom of the second transonic dip.

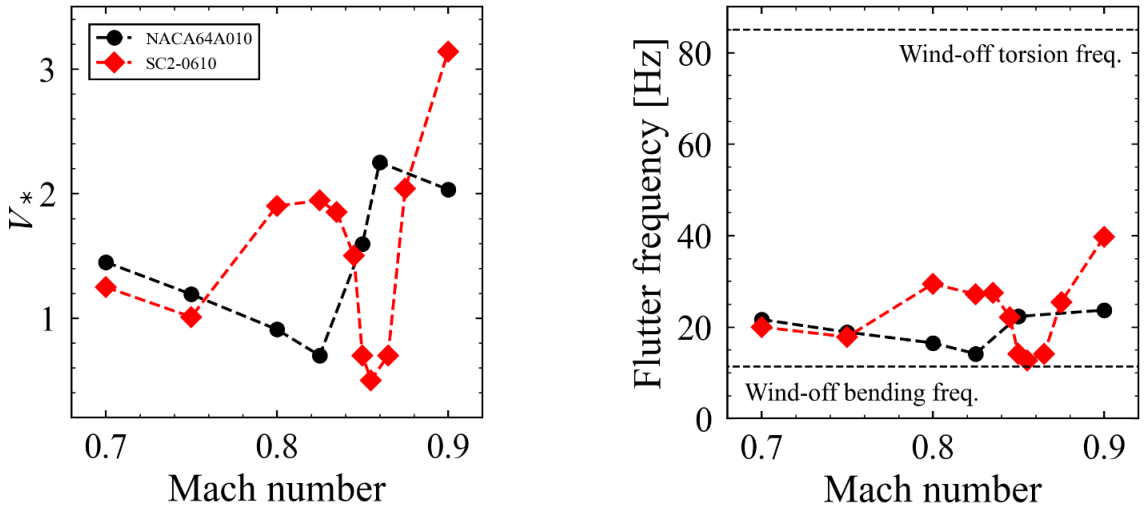

(a) Speed index (b) Flutter frequency

Fig. 3 – Flutter characteristics of NACA64A010 and SC2-0610 airfoils

(a) $M_\infty = 0.75$ (b) $M_\infty = 0.8$

Fig. 4 – Mach number distributions for the SC2-0610 airfoil at the steady-state (non-oscillating) condition around the 1st-dip.

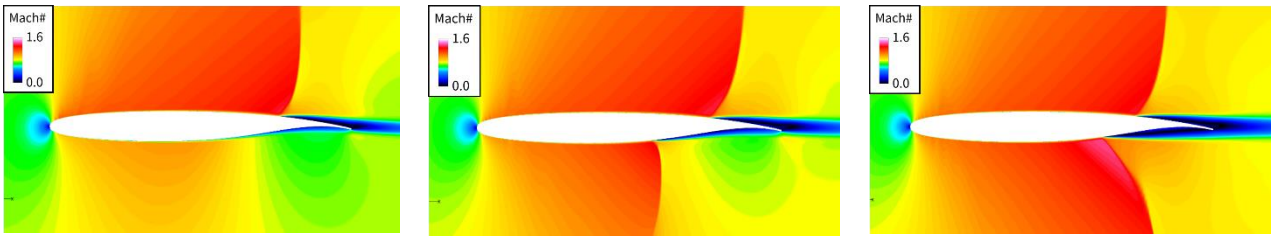

(a) $M_\infty = 0.825$ (b) $M_\infty = 0.855$ (c) $M_\infty = 0.875$

Fig. 5 – Mach number distributions for the SC2-0610 airfoil at the steady-state (non-oscillating) condition around the 2nd-dip.

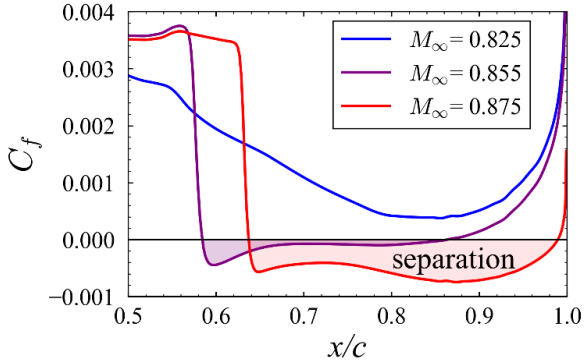

Fig. 6 – Skin friction distribution for the SC2-0610 airfoil on the lower surface around the 2nd-dip.

3.2 Double transonic dip mechanism in a supercritical airfoil

An analysis using a forced oscillation airfoil was performed to investigate the unsteady behaviors of shock wave and separation over the lower surface of the SC2-0610 airfoil. As was shown in Fig. 3(b), the flutter occurred in the first bending mode at the bottom of the second transonic dip ($M_\infty = 0.855$). Thus, the forced pitching oscillation similar to the first bending mode was adapted. The pitching motion α is given as follows:

$$\alpha = \alpha_0 \cos\left(\frac{2U_\infty k}{c} t\right), \tag{5}$$

where α_0 is the oscillation amplitude, k is the reduced frequency, and t is the time. The pitching center is located at $x = -0.5c$ (see Fig. 1). The oscillation amplitude is 1 degree, and the reduced frequency is 0.2. These parameters represent the airfoil motion on the flutter boundary at $M_\infty = 0.855$.

Figure 7 shows the phase difference of lift coefficient for the variation of the airfoil motion (Eq. (5)). Generally, when the phase of lift force is delayed (i.e., the phase difference is negative), the airfoil motion becomes unstable. On the other hand, when the phase of lift force is advanced (i.e., the phase difference is positive), the airfoil motion becomes stable. The results show that the phase delay only happens at $M_\infty = 0.855$, suggesting that the airfoil motion at $M_\infty = 0.855$ could be the most unstable among three Mach number conditions. The condition of at $M_\infty = 0.855$ corresponds to the bottom of the second transonic dip.

Figure 8 shows the phase difference of surface pressure coefficient on the lower surface. Here, the first harmonic component of surface pressure coefficient with respect to the pitching motion is defined as follows:

$$Cp = Cp_0 \cos\left\{\frac{2U_\infty k}{c} t + \theta(Cp)\right\}, \tag{6}$$

where Cp is the pressure coefficient on the lower surface, Cp_0 is the amplitude of Cp variation, and $\theta(Cp)$ is the phase difference of surface pressure coefficient. The phase-advanced region is dominant over the lower surface at $M_\infty = 0.825$ and $M_\infty = 0.875$, while at $M_\infty = 0.855$, the phase-delayed region appears over the lower surface, particularly behind the shock wave. Thus, the result suggests that the flow behaviors behind the shock wave determine the phase-delayed or phase-advanced feature of the lift coefficient.

Figure 9 shows the variation of skin friction distribution on the lower surface during the oscillation. The distributions at $M_\infty = 0.855$ demonstrate that the flow separation and reattachment occur in the region behind the shock wave during the pitching oscillation. On the other hand, the boundary layer at $M_\infty = 0.825$ is attached during the oscillation and the boundary layer is fully separated during the oscillation at $M_\infty = 0.875$. Therefore, the results indicate that the phase-delayed feature may be caused by the separation and reattachment cycle over the lower surface during the oscillation.

4. Conclusion

A two-dimensional transonic flutter analysis was performed using a conventional symmetric airfoil (NACA64A010) and a supercritical airfoil (SC2-0610). The following conclusions were drawn:

1. The double transonic dip on the flutter boundary was captured with the supercritical airfoil
2. The first transonic dip is a typical transonic dip, which was caused by the shock wave appearance over the upper surface
3. The second transonic dip was triggered by the shock wave generation over the lower surface
4. The separation and reattachment cycle caused the phase-delayed feature of aerodynamic forces, and thus determined the bottom of the second transonic dip.

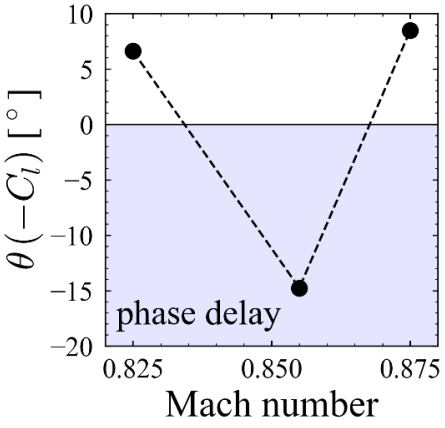

Fig. 7 – Phase difference of lift coefficient for SC2-0610 airfoil around the 2nd-dip.

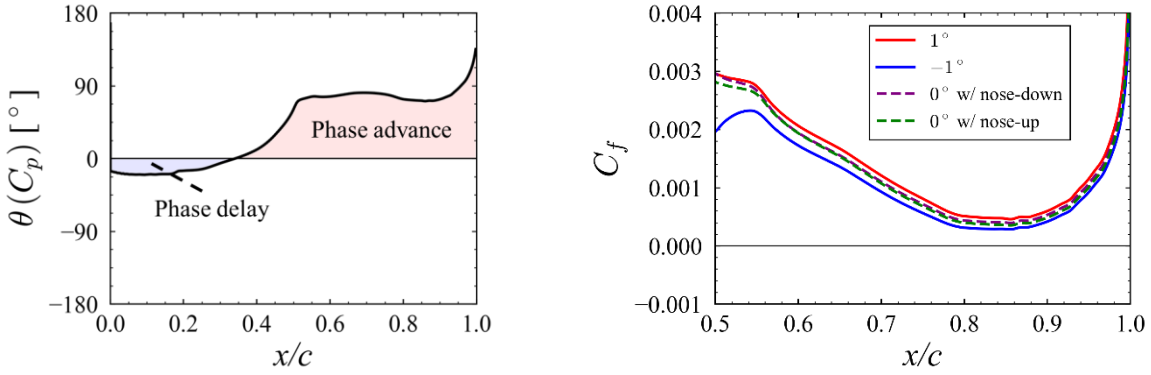

(a) $M_\infty = 0.825$

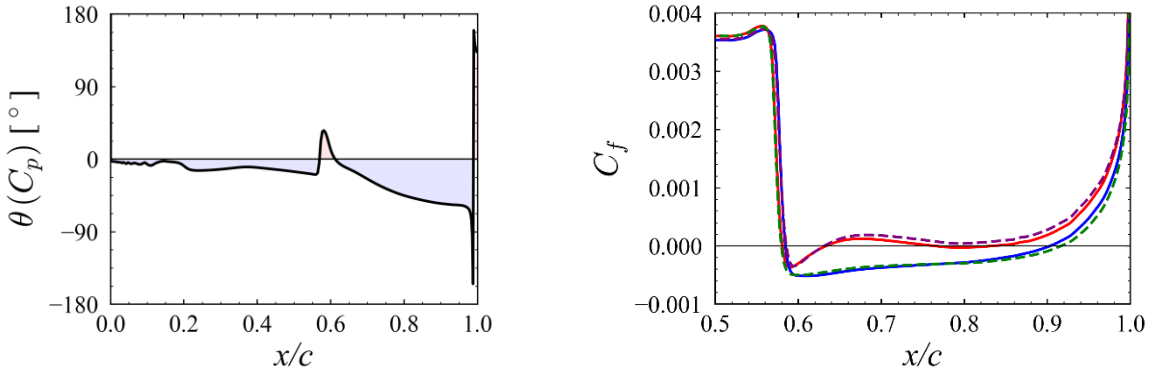

(b) $M_\infty = 0.855$

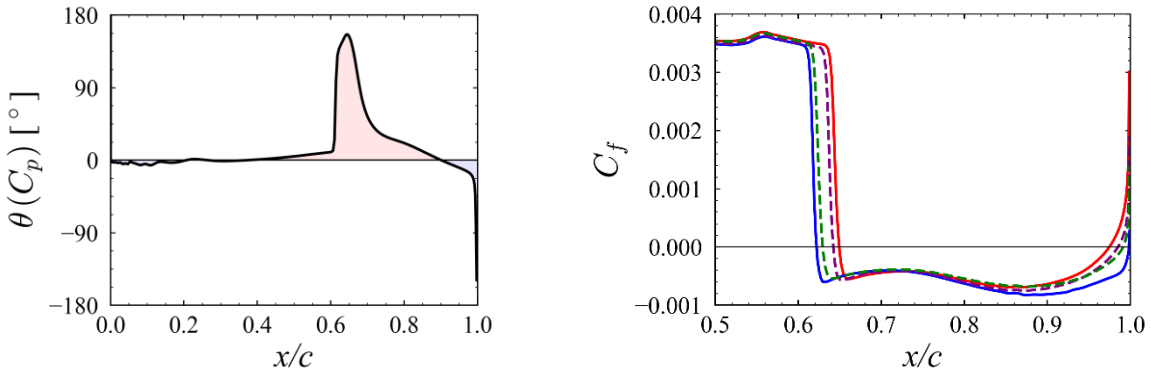

(c) $M_\infty = 0.875$

Fig. 8 – Phase difference of surface pressure coefficient for SC2-0610 airfoil on the lower surface.

Fig. 9 – Skin friction distribution for SC2-0610 airfoil on the lower surface during the pitching oscillation.

5. Contact Author Email Address

mailto: toma@eis.hokudai.ac.jp

6. Copyright Statement

References

[1] Nakamichi J, Tamayama M., and Kodama S. *Aeroelasticity (Japanese)*. 1st edition, Maruzen Co, 2019.

[2] Mykytow, W.J. *A Brief Overview of Transonic Flutter Problems*. AGARD conference proceedings, No. 226, pp. 11-1-11-11, 1997.

[3] Farmer, M.G., Hanson, P.W., and Wynne, C.E. *Comparison of supercritical and conventional wing flutter characteristics*. NASA Technical Memorandum, 72827, 1976.

[4] Bohbot, J., Garnier, J., Toumit, S., and Darracq, D. *Computation of the Flutter Boundary of an Airfoil with a Parallel Navier-Stokes Solver*. *AIAA paper,* 2001-0572, 2001.

[5] Rivera, A.J., Dansberry, B.R., and Bennett. R.M. *NACA0012 benchmark model experimental flutter results with unsteady pressure distributions*. NASA Technical Memorandum, 10751, 1992.

[6] Bendiksen, O.O. *Modern developments in computational aeroelasticity*. *Journal of Aerospace Engineering*, Vol. 218, pp. 157–178, 2004.

[7] Nakamichi, J. *Some Computations of Unsteady Navier-Stoles Solutions Around Oscillating Airfoils*. NASA Technical Memorandum, 88341, 1986.

[8] Isogai, K. *On the Transonic-Dip Mechanism of Flutter of a Sweptback Wing*. *AIAA Journal*, Vol. 17, No. 7, pp. 793–795, 1979.

[9] Yates, E.C. Jr. *AGARD Standard Aeroelastic Configurations for Dynamic Response - Wing 445.6*. NASA Technical Memorandum, 100492, 1988.

[10] Shima, E., and Jounouchi, T. *Role of CFD in Aeronautical Engineering (No. 14)–AUSM type Upwind Schemes*. *Proceedings of the 14th NAL Symposium on Aircraft Computational Aerodynamics*, SP-34, pp. 7–12, 1997.

[11] Anderson, W.K., Thomas, J. L., and van Leer, B. *Comparison of finite volume flux vector splittings for the Euler equations*. *AIAA Journal*, Vol. 24, No. 9, pp. 1453-1460, 1986.

[12] Van Albada, G.D., van Leer, B., and Roberts, W.W. *A comparative study of computational methods in cosmic gas dynamics*. *Astronomy and Astrophysics*, Vol. 108, pp. 76-84, 1982.

[13] Yoon, S., and Jameson, A. *Lower-Upper Symmetric-Gauss-Seidel Method for the Euler and Navier-Stokes Equations*. *AIAA Journal*, Vol. 26, No. 9, pp. 1025–1026, 1988.

[14] Spalart, P.R., and Allmaras, S.R. *A one-equation turbulence model for aerodynamic flows*. *AIAA Paper*, Vol. 1, pp. 5–21, 1994.

[15] Davis, S. S., and Malcolm, G. N. *Transonic shock-wave/boundary-layer interactions on an oscillating airfoil*. *AIAA Journal*, Vol. 18, No. 11, pp. 1306–1312, 1980.